01 Mar 2022

Component Repair using Additive Manufacturing: Experiments and Thermal Modeling

Lan Li

Xinchang Zhang

Tan Pan

Frank W. Liou
Missouri University of Science and Technology, liou@mst.edu

Recommended Citation

L. Li et al., "Component Repair using Additive Manufacturing: Experiments and Thermal Modeling," *International Journal of Advanced Manufacturing Technology*, vol. 119, no. 1 thru 2, pp. 719 - 732, Springer, Mar 2022.
The definitive version is available at https://doi.org/10.1007/s00170-021-08265-y

The International Journal of Advanced Manufacturing Technology (2022) 119:719–732
https://doi.org/10.1007/s00170-021-08265-y

ORIGINAL ARTICLE

Component repair using additive manufacturing: experiments and thermal modeling

Lan Li[1] · Xinchang Zhang[1,2] · Tan Pan[1] · Frank Liou[1]

Received: 14 July 2021 / Accepted: 21 October 2021 / Published online: 8 November 2021

Abstract
The objective of this work is to propose an advanced automated damage detection and damage reconstruction algorithm for damaged gear tooth repair. It can automate tool path design and provide precise repair volume detection for complex repair volume. First, models of the damaged and nominal parts were obtained by reverse engineering. Next, the damaged model was aligned with the nominal model. After that, both models were sliced into layers, and a set of parallel and equidistant casting rays was used to intersect with these layers to extract the repair volume. Then the repair tool path was generated and used to guide the laser additive manufacturing process for repair. The corresponding repair experiment and validated numerical model based on repairing a complex gear fracture was conducted to evaluate the reconstruction algorithm efficiency and repair part quality. Microstructure analysis and Vickers hardness test were carried out to evaluate the repaired part quality. The coincidence of scanning points between repaired model and the nominal model is high. The repair experiment confirmed the strong efficiency of this repair algorithm for complex geometry repair. A 3D finite element model was also developed to simulate the repair process and provide critical deformation and residual stress of the repaired parts. The predicted temperature and residual stress results were compared and showed a good agreement with the experimental measurements. These results further validated that the proposed repair algorithm and simulation model are suitable and efficient for the automated repair of damaged components.

Keywords Damage detection and reconstruction · Direct metal deposition · Repair · Microstructure analysis · Deformation and stress

1 Introduction

Metallic components are widely used in mechanical systems. For instance, aero-engines consist of compressors, combustors, turbines, nozzles, etc., which are mainly made of metallic materials such as Ti-6Al-4V and nickel-based alloys [1]. Transmissions contain a complex series of gears, clutches, etc. that are made of high-strength steel or nickel alloys [2]. These metallic parts form the most important section in mechanical systems, and their life directly affects the reliability of these systems. However, many metallic components usually work in a harsh environment. For example, aero-engine turbine blades often work at an elevated temperature and pressure environment and have a high likelihood of impact with foreign objects such as rocks [3]. Gears are generally subjected to heavy loading, high temperature, and wear. The harsh working environment can easily damage these parts prematurely, resulting in many types of defects such as creep damage, erosion, and fracture [4]. Unfortunately, most critical metallic parts are made of high-performance materials such as Ti- or Ni-alloys, and they are costly due to the difficult and complex manufacturing processes. Therefore, when they are damaged, discarding them and replacing them with new parts will cost significantly. A cost-efficient alternative is to repair them and put them back to service after complete inspection [5–7]. Repair-damaged components can considerably extend their life and also avoid interruption in the production process, especially for parts that replacement is no longer available.

Laser-aided direct metal deposition (LDMD) process has emerged and has shown great applications in the field of

✉ Xinchang Zhang
xz25c@mst.edu

[1] Department of Mechanical and Aerospace Engineering, Missouri University of Science and Technology, Rolla, MO 65409, USA

[2] Idaho National Laboratory, Idaho Falls, ID 83415, USA

repair [8, 9]. The advantages of LDMD make it suitable for repair. For example, LDMD introduces low heat and can cause less distortion of the base part, which is perfect for dimensional-delicate thin-wall structures. In addition, LDMD can fabricate full-dense parts with high strength. In the LDMD process, a concentrated high-energy laser is used to create a melt pool on the damaged zone, and in the meantime, incoming metal powders are delivered into the melt pool and undergo melting and solidification to form a layer. Because the substrate material was melted and mixed with the incoming material, an excellent bond can be achieved [10, 11].

Reconstructing the repair volume to generate the repair tool path is essential for remanufacturing since it provides the geometry that needs to be precisely recreated on the damaged region. Several researchers have studied the LDMD process for component repair following a manually defined tool path. Pinkerton et al. [12] made two different geometries on H13 hot-work tool steel substrates and restored the damaged area with H13 powders of high quality. Wilson et al. [13] employed the LDMD process to restore a damaged turbine blade and then validate the strength of the repair by tensile tests. LDMD processes can also process other materials to repair missing volumes including Ti-6Al-4V [14–16] and stainless steel [17]. However, the repair objects in the aforementioned studies were very simple and geometric regular since the repair volumes were easy to predict. In this scenario, it is able to generate a tool path manually. However, in most situations, the repair volume is very complex and unique, which requires numerous amounts of time to manually define the tool path. In addition, the operator's experience-based damage reconstruction cannot guarantee consistent and repeatable repair quality. Both factors dramatically increase the risk of failure during service. Therefore, an automated damage reconstruction strategy is required, which guarantees time-saving and precise part repair. In previous studies [18–20], we proposed an engineering algorithm to reconstruct the fracture surface on the damaged model and cut the nominal model to restore the missing volume on damaged parts. These experiments were on good evaluation for the automated repair process. However, this process limits fast repair due to inefficient scanning points on damaged surfaces for automated path plan, especially for complicated gear geometry and tooth fracture surface. Therefore, developing a high-efficient damage reconstruction strategy by assuring good deposits is urgently needed in modern repair workshops. Here gives the objective of this study. The advanced automated damage detection and reconstruction algorithms for much more scanning points were proposed in this study for component repair of complicated gear with tooth fracture. Moreover, mechanical testing and modeling were used to validate the automated repair process.

In this work, an advanced reconstruction algorithm was proposed to automatically and efficiently restore the missing geometry with SS304L powder on a Fe-based damaged gear tooth. In Section 2, three steps are elucidated to design the tool path. Firstly, the damaged gear model was compared with the nominal model. Secondly, missing geometry was obtained by slicing the required volume into several layers. Finally, the tool path was generated. In Section 3, laser scanning tracks in eight layers were generated according to the extracted geometry and appropriate LDMD process parameters. SS304L powder particles were deposited on the damaged region performed with the LDMD process. Microstructure analysis and Vickers hardness test were carried out to evaluate the repaired part quality. In Sections 4 and 5, based on the repair volume and scanning layers, a thermo-mechanical numerical model was developed to accurately predict the deformation and stress behavior of the repair process. Finally, conclusions were drawn about the automated damage reconstruction method and simulation model.

2 Repair volume reconstruction

Defining the repair volume is the first step in the repair process so that the missing geometry can be defined and deposited back on the damaged parts. A gear with module 2 and teeth 20 was used to exemplify the repair volume reconstruction process. In this process, the nominal part is scanned to reconstruct the nominal model as shown in Fig. 1a. After that, a defect was created on one tooth and the damaged model was reobtained as shown in Fig. 1b. For repairing the damaged gear, it is crucial to reobtain the geometry of the missing tooth since the tool path in the deposition process is generated according to the missing geometry.

In the real repairing process, the model of the damaged part was generally obtained using reverse engineering-based tools such as coordinate measuring machines (CMM) or 3D scanners. Laser scanners or structured-light scanners can reconstruct the 3D model of an existing object very rapidly and with high accuracy and, therefore, are widely used in repair applications. Researchers reported that 3D-scanned damaged models were skewed from the nominal models. It is because the separate scanning process of nominal and damaged models disarranges the position of both models. It is of considerable importance to align the damaged model with the nominal model to reconstruct the missing volume. For mimicking the disorder of both models, the damaged model shown in Fig. 1b was rotated around x, y, and z axis with random angles. This results in the arbitrary position of both models as illustrated in Fig. 1c. An algorithm was proposed to generate the transformation matrix to align both models together.

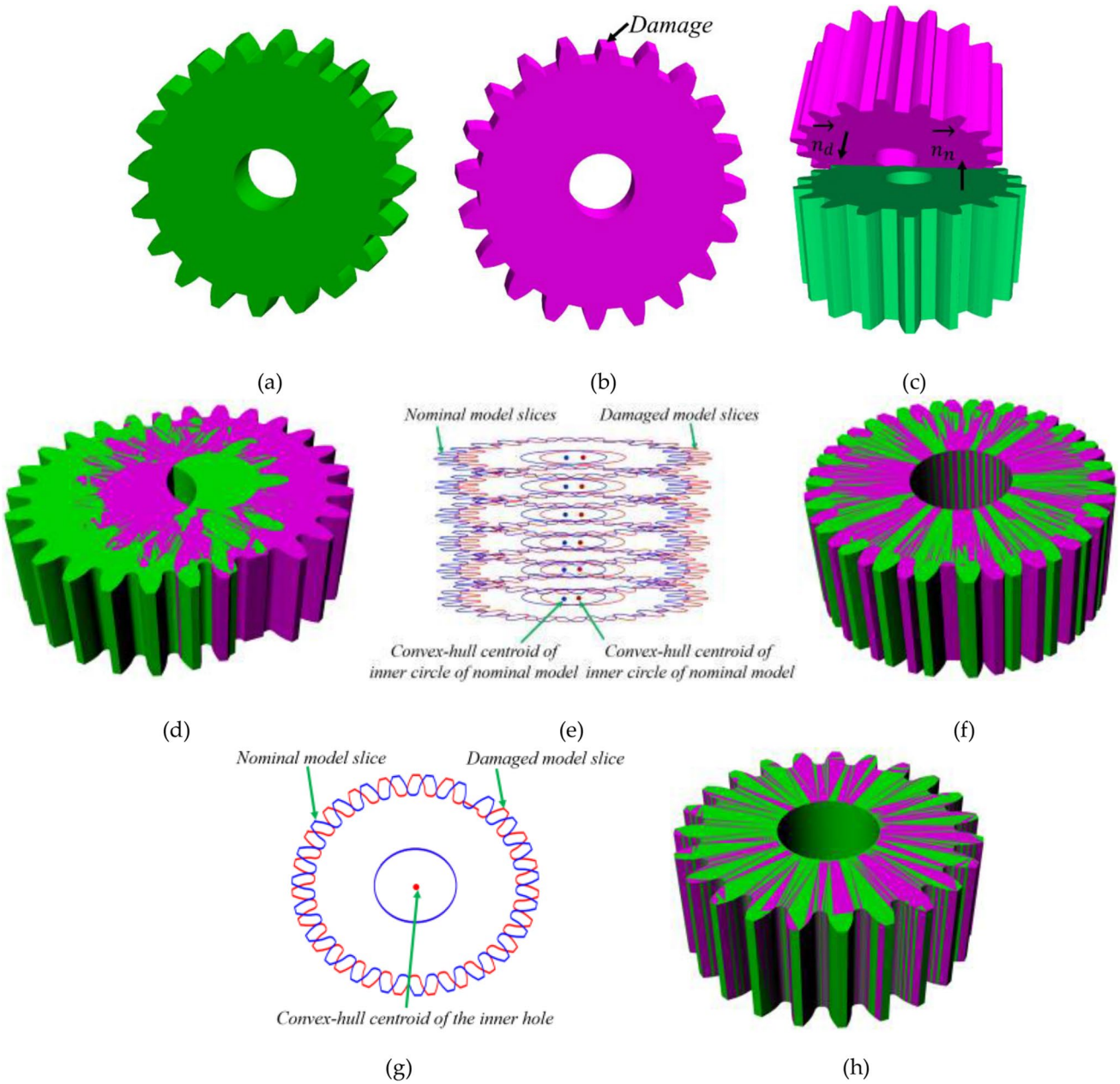

Fig. 1 Nominal (**a**) and damaged (**b**) models of the gear. (**c**) Nominal and damaged models in unaligned condition. (**d**) Models after surface alignment. (**e**) Cross-sections and convex-hull centroid of the inner hole for nominal and damaged models. (**f**) Models after convex-hull centroid alignment. (**g**) A slice from nominal and damaged models. (**h**) Fully aligned model

The model alignment was carried out in the following sequence. The first step which was named surface alignment was to align the side surfaces of both models. The normal vectors of the side surfaces of both models were searched, and then the transformation matrix was calculated to ensure the coincidence of both normal vectors. As an example, the normal vector of the target surface of the nominal model is $n_n=(x_n, y_n, z_n)$, and the normal vector of the damaged model is $n_d=(x_d, y_d, z_d)$, shown in Fig. 1c. The objective was to obtain the transformation matrix T so that $n_d \bullet T = n_n$. The transformation matrix T was obtained through Rodrigues' rotation formula. After this step, the relative position and orientation of both models are shown in Fig. 1d. It is obvious from Fig. 1d that although the two side surfaces were aligned, both models were not aligned completely. In the second step which is convex-hull centroid alignment, both nominal and damaged models were sliced into a number of layers as shown in Fig. 1e. It should be noted that, because a broken tooth was on the damaged model, the convex-hull centroids of the outer profile of the damaged model cannot

be used for alignment purposes. This is because the damaged tooth will shift the convex-hull centroids. However, since the inner hole on the damaged model is intact, the convex-hull centroids of the inner hole can be used for alignment. Based on the coordinates of the convex-hull centroids, a translation vector can be obtained to translate the damaged model to the position as shown in Fig. 1f. Figure 1g shows a cross-section from the nominal and damaged models after convex-hull centroid alignment. It shows the damaged model is still not aligned with the nominal model. By rotating the damaged model around the convex-hull centroid, the damaged model can be eventually aligned with the nominal model. The target is to obtain the rotary angle that the damaged model should perform. The optimal rotary angle was obtained by maximizing the overlapping area of the two cross-sections as shown in Fig. 1g. Figure 1h illustrates the finally aligned models.

After model alignment, repair volume reconstruction was conducted to reobtain the missing geometry. For such purpose, an area covering the damage was selected as shown in Fig. 2a. After that, casting rays in three directions (x, y, and z) were injected to intersect both models. Such casting rays intersected with the selected area of the nominal model and the damaged model and the intersections are shown in Fig. 2c and d, respectively. The intersections forming the repair volume were obtained as follows. As shown in Fig. 2b, the intersections of casting rays with the nominal model cross-section are $[a, a', b, b', c, c', d, d', e, e', f, f', g, g', h, h']$. For the damaged model, since there is a missing geometry, the intersections are $[h, h']$. Therefore, it can be seen that $[a, a', b, b', c, c', d, d', e, e', f, f', g, g']$ are missing from the damaged model and should be reconstructed. Using this strategy, the missing points were obtained as shown in Fig. 2e. Such point data were further processed to generate the STL model as shown in Fig. 2f. The reconstructed repair volume was positioned on the damaged model to test the accuracy as shown in Fig. 2g, which confirms that the missing geometry has been successfully restored.

3 Gear repair experiment and results

3.1 Experiment procedure and material preparation

In this study, the LDMD system (Fig. 3a–d) consists of a laser nozzle system with a maximum power of 1000 W, a blown powder feeding system, and a 3-axis CNC work table to realize the relative movement between the substrate

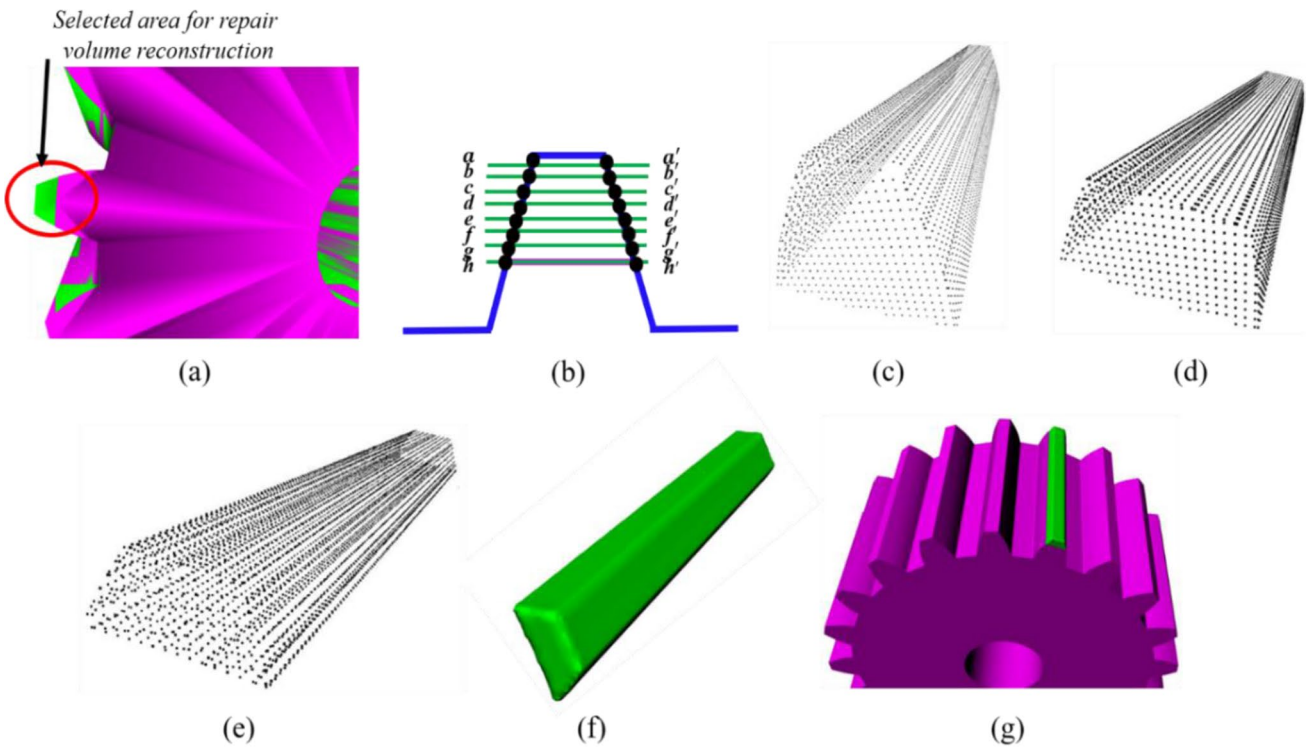

Fig. 2 Repair volume reconstruction. (**a**) Selected area for repair volume reconstruction. (**b**) Schematic diagram showing the repair volume reconstruction strategy. (**c**) Intersections of casting rays with the nominal model. (**d**) Intersections of casting rays with the damaged model. (**e**) Extract point set forming repair volume. (**f**) Reconstructed STL model of the repair volume. (**g**) Repair volume positioned on the damaged model

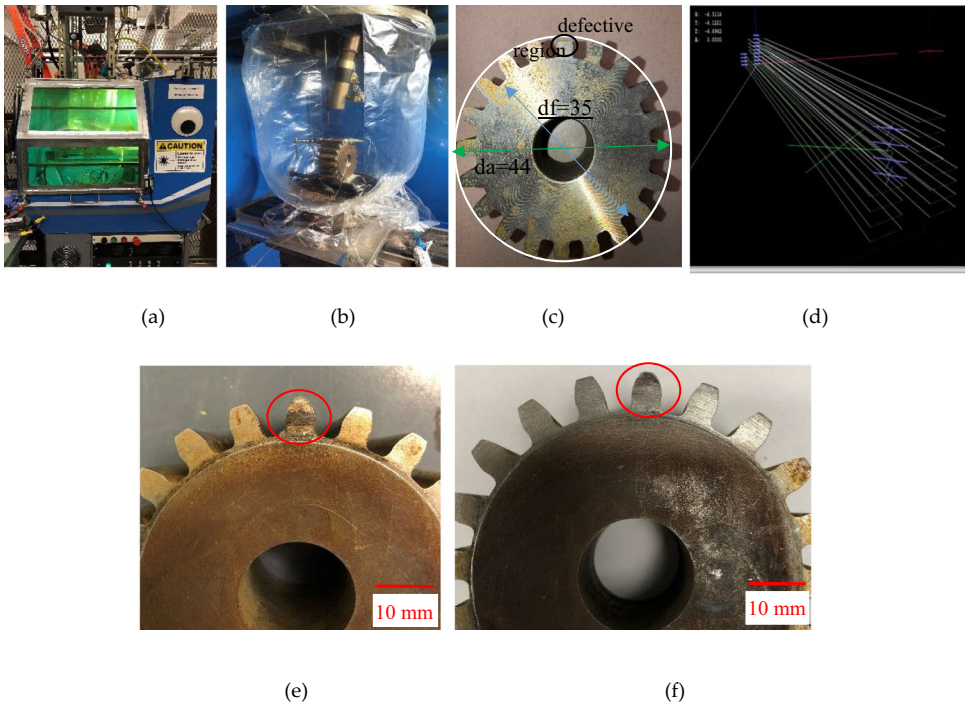

Fig. 3 LDMD equipment to perform the repair experiment (**a**) LDMD system chamber. (**b**) LDMD experimental set-up. (**c**) Damaged gear. (**d**) Tool path generation for material deposition. (**e**) Gear after LDMD process. (**f**) Gear after machining

Table 1 Processing parameters for repair experiment

Experiment parameters	Values
Power, *P* [W]	850
Powder flow rate, [g/min]	2.8
Scan speed, [mm/min]	210
Laser diameter, *d* [mm]	1.3
Layer thickness, [mm]	0.25
Number of laser tracks, *N*	28

and the laser beam. The maximum laser beam diameter is 2 mm. Argon shielding gas is inserted to preclude material oxidization.

Recall that automated damage detection and reconstruction algorithms were completed for the damaged gear in Section 2. In this step, the missing geometry in the damaged gear was separated into eight layers. The diameter of repair gear with module M=2 and teeth N=20 was given in Fig. 3c. The outside diameter is 44mm and the root diameter is 39mm. The whole depth of the gear is 4.5mm which was fractured at a height of 2.5 mm. Considering a total thickness of 2 mm to be deposited, each layer was planned for a thickness of 0.25 mm. An outline contour with a zigzag infill pattern was used in this study. That is, laser scans along the z-axis and then follow a zigzag pattern. The tool path was referred to by the extracted points in Fig. 3d. The processing parameters were listed in Table 1. Powder flow rate and corresponding laser power are calculated from the defined repair volume raised by this reconstruction algorithm. The damaged area was firstly cleaned with acetone and then deposited by SS304L powder particles. The experimental powder of SS304L alloy had a spherical shape and the particle diameter is in the range of 25–100 µm.

3.2 Repair efficiency and sample preparation

Figure 3e and f show the gear after metal deposition and post-machining. Again, scanning of the repaired model after metal deposition was obtained and was aligned with the nominal model. The coincidence is about 99.6% which is much higher than the literature [19, 20]. That can be explained that this advanced reconstruction algorithm rises more scanning points for component repair. Even for this complex repair volume, the post-machining amount of time from this automated define tool path is much less than paper [20]. It can guarantee consistent and repeatable complex damage reconstruction, thus dramatically decreasing the risk of failure during service. Therefore, this advanced automated damage reconstruction strategy is time-saving and efficient for repairing complex geometry including the automated tool path planning and low mis-integration. The microstructure analysis of the as-deposited SS304L around the bounding area was conducted to assess the repair quality. After fabrication, the specimen was cut, polished, and then etched with 60/40 nitric acid and finally captured using HIRO KH-8700 (HIROX, Hackensack, NJ, USA) digital optical microscope and a Helios NanoLab 600 (Thermo Fisher Scientific, Waltham, MA, USA) scanning electron microscopy (SEM).

3.3 Microstructure evaluation

Micrographs were taken at three different cross-sections of the repaired samples: near the bonding area (Fig. 4a), the deposits near the bonding area (Fig. 4b), and the deposits on the as-deposited top site (Fig. 4c). It was noticed that the bonding interface between the deposited material and the substrate was very clear. Fabrication defects such as delamination, pores, and cracks were not detected on the bonding interface. Good metallurgical bonding at the interface was further confirmed by microstructure analysis. It was noticed that columnar dendrites arrange normal to the layer band interface since this is towards the maximum temperature gradient. As can be seen from Fig. 4b and c, a large columnar microstructure was observed right above the interface and in the heat-affected zone (HAZ). This is due to the deposit process that the substrate material near the interface was melted with the delivered SS304L and then subsequently re-solidified by the successive depositing layers. Some cellular structures were also noticed in such regions. The result of cellular grain structure in this sample was consistent throughout the built samples. The cellular grain structure seen in these micrographs and further identified by Fig. 4c confirmed the fast cooling rate of a cellular solidification structure. The microstructure of the top zone mainly consists of clusters of cells, as shown in Fig. 4c.

3.4 Vickers hardness analysis

The hardness measurement was performed on the cross-section of the repaired sample from deposits to substrate using a Struers Duramin 5 microhardness tester. Figure 4d plotted the hardness distribution at different locations of three samples. Indentions started at the substrate region

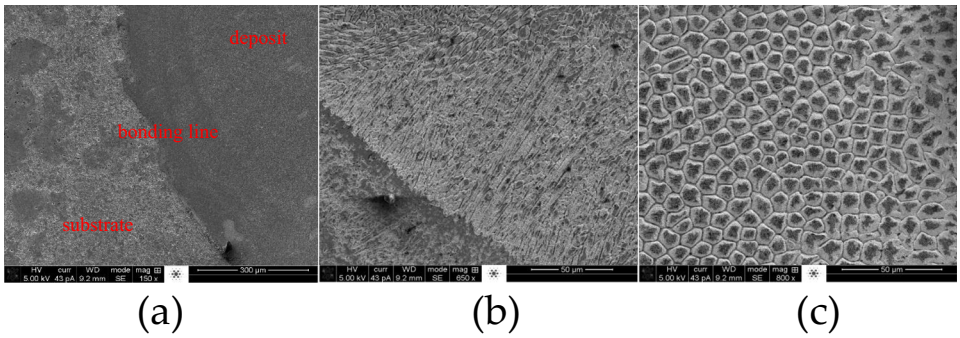

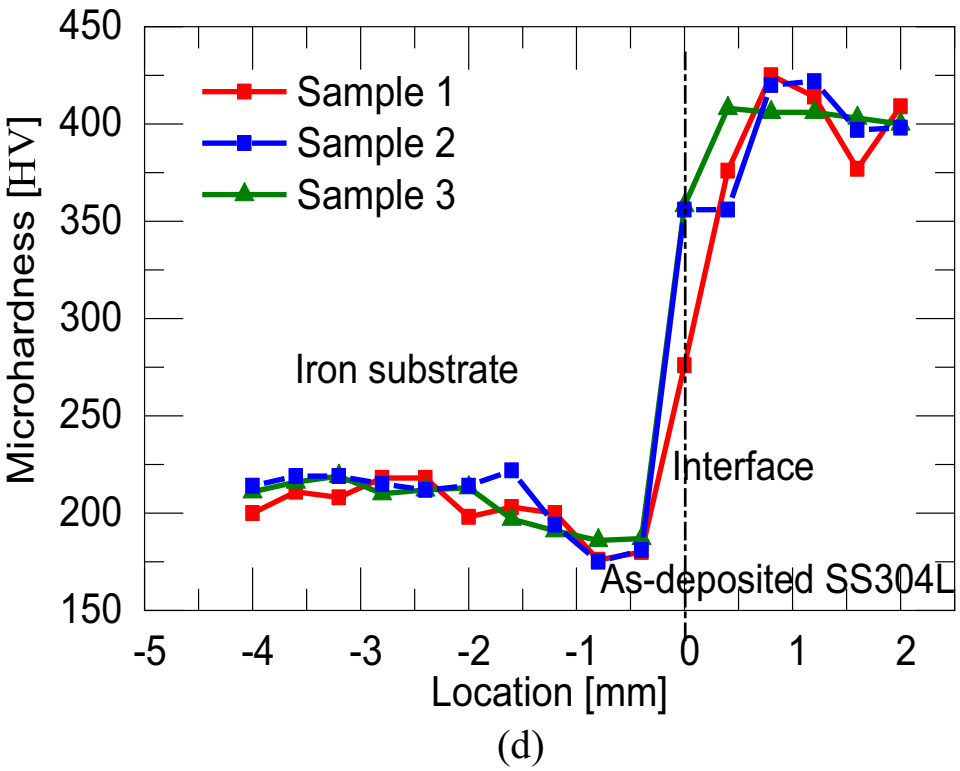

Fig. 4 (**a**) Micrographs on the cross-section of materials on the bonding area. (**b**) Microstructure on deposits near the bonding area. (**c**) Microstructure on deposits away from the bonding area. (**d**) Vickers hardness distribution

and continued at various spacing into the SS304L region. The interval between two indentations was set to 0.5 mm. The hardness on the substrate side had relatively constant hardness values between 180 HV and 230 HV, which is lower than that of deposit sides because bulk low carbon steel hardness is smaller than 304 SS. On the other side, at the interface, the deposited material goes as low as 180 HV and increases to over 400HV around 0.75 mm. It was also found that the hardness of deposits decreased slightly as the deposition layer increased. This was attributable to the fine microstructure in lower deposit layers compared with higher layers. The microstructure growth speed for each individual layer gradually reduces as deposited layers increase, which is attributable to microstructure growth of the formed parts and can further validate the hardness variation. To identify the size of microstructure in the deposition height, optical microscopy and scanning electron microscopy (SEM) were applied in Fig. 4b and c as we discussed in the last section. Thus, the hardness at as-deposited material near the interface was slightly higher than that away from the interface.

4 Numerical analysis of the laser repair process

During the additive manufacturing process, significant thermal residual stresses and distortion can be induced by moving high-intensity lasers. High thermal residual stress is a critical issue since it is likely to cause distortion, cracking, and fatigue failure and hence impacts the quality of the repaired product. The deformation and stress distribution in the additive manufacturing process can be simulated by the finite element method (FEA) with specified material properties and boundary conditions. Commercial FEA software such as ABAQUS®, COMSOL Multiphysics®, and ANSYS® can be used to optimize design parameters to meet specific performance [21–28]. Therefore, it is necessary to track the residual stress evolution during and after the repair in order to achieve successful part printing for complex 3D components.

4.1 Model set-up

The aim of FEA modeling in this section is to calculate residual stress and deformation distribution in the repaired sample. A 3D-coupled thermo-mechanical model was developed by ANSYS® Mechanical APDL to simulate the LDMD process of the gear repair in which the temperature history and residual stress can be instantly monitored. In this commercial software, the energy input, material deposition, deposition rate, substrate preheating, and tool paths during the deposition process are implemented by user subroutine in APDL. In the model, the transient heat transfer analysis was firstly run to obtain temperature distribution. Then, the structural analysis was implemented to calculate thermal stress and distortion.

Figure 5a shows the geometry of damaged gear as a modeling domain. The intact section with the damaged tooth is shown in Fig. 5b and c . Twenty-eight tracks were planned for the total LDMD process. The laser traversed at a speed of 210 mm/min. In the material deposition process, the continuously adding elements are implemented by the birth-and-death function in ANSYS® to activate an element. This element activation method is widely used in modeling material

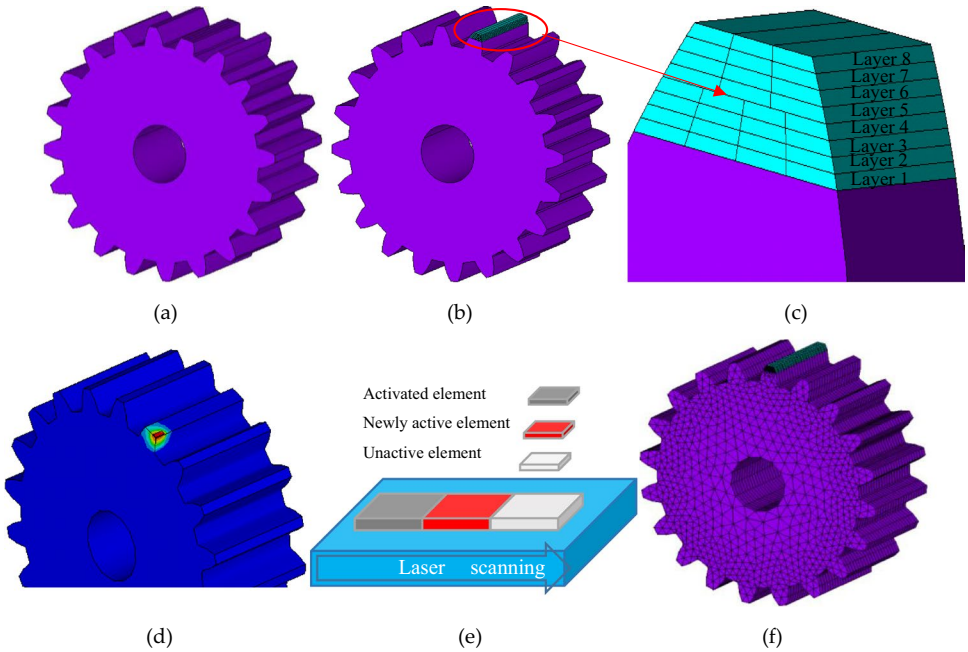

Fig. 5 (**a**) FEA model geometry of the damaged gear. (**b**) Laser scan strategy of 4 tracks of repair volume. (**c**) A zoomed-in view of the repair with deposit track. (**d**) FEA model of the first deposition of the damaged gear. (**e**) Schematic of element birth and death function. (**f**) Finite element mesh for LDMD process simulation

deposition in AM process. Figure 5d and e show material addition during the LDMD process by the element birth and death function. At the initial state, just the substrate elements were all activated. The element with 0.25-mm thickness for new material addition was activated sequentially in the laser scanning direction to simulate the material addition process. Other processing parameters are the same as the laser repair experiment. To reduce the computational cost, the deposited elements use hexahedral mesh with 0.5 mm, and the gear base part was coarsely meshed. The final model contained a total of 56,650 elements and 43,993 nodes. The finite element mesh for the LDMD process simulation is shown in Fig. 5f.

4.2 Governing equation for thermo-mechanical analysis

The transient energy equation is used as the governing equation for heat transfer in the entire volume of the material, given as

$$\rho c_p(T)\frac{\partial T}{\partial t} = \frac{\partial}{\partial x}\left[k(T)\frac{\partial T}{\partial x}\right] + \frac{\partial}{\partial y}\left[k(T)\frac{\partial T}{\partial y}\right] + \frac{\partial}{\partial z}\left[k(T)\frac{\partial T}{\partial z}\right] + \dot{q} \tag{1}$$

where T is the current temperature; $k(T)$ is the temperature-dependent thermal conductivity; $c_p(T)$ is the temperature-dependent specific heat; ρ is the constant density; $\dot{q}$ represents heat sink or source in the volume; t is the time; and x, y, and z are the coordinates in the reference system as the same as X, Y, Z in graphs.

Stress equilibrium equation is used as the governing equation for mechanical analysis [29, 30]:

$$\nabla \cdot \sigma = 0 \tag{2}$$

where σ is the second-order stress tensor associated with the material behavior law.

The isotropic Hooke's law is used to relate stress and elastic strain as

$$\sigma = C\varepsilon^e \tag{3}$$

where ε^e is the second-order elastic strain tensor and C is the fourth-order material stiffness tensor.

Thermo-elasto-plasticity is considered in the deposition process. Therefore, the total strain ε has three components [31]:

$$\varepsilon = \varepsilon^{th} + \varepsilon^p + \varepsilon^e \tag{4}$$

$$\varepsilon^{th} = \alpha \cdot \triangle T \tag{5}$$

where ε^{th}, ε^p, and ε^e are the thermal strain, plastic strain, and elastic strain, respectively; α is the coefficient of thermal expansion; and ΔT is the temperature difference with respect to the reference temperature. The thermal strain is calculated by Equation (5). Elastic and plastic strain in our study is calculated by the bilinear isotropic hardening model, which is defined by elastic modulus E, Poisson's ratio ν, yield strength σ_Y, and tangent modulus G [32, 33].

4.3 Modeling of the heat source

In experiments, the laser beam heats the layered material in a circular influencing region. In the simulation, this heating process is represented as volume heat flux on the active element of powder. ANSYS Mechanical does not have a GUI tool to create functions that depend on more than one variable. Instead, insert APDL commands in ANSYS Mechanical was used as the user subroutine to implement the energy input. Because of the small dimension in the powder depth direction, the power density in the depth direction does not change in the layer thickness direction. The heat flux obeys Gaussian distribution on the x-y plane which follows as:

$$\dot{q} = \frac{2\phi P}{\pi r_0^2}\exp\left[-2\frac{r^2}{r_0^2}\right] \tag{6}$$

where ϕ is the laser absorptivity and $\phi = 0.3$ in this work. r_0 is the radius of the laser beam and P is the laser power. Equation (6) shows that heat flux exponentially decays away from the laser beam center in the x-y plane.

4.4 Boundary conditions

Before the laser heating, the atmospheric temperature is set as the initial temperature condition. The substrate follows the uniform temperature distribution:

$$T(x, y, z, t)_{t=0} = T_0 = T_a \tag{7}$$

where T_a is the ambient temperature equals the initial temperature T_0, set as 25 °C.

All external surfaces of the deposited layer are exposed to the atmosphere and are subjected to heat convection with air and heat radiation. These two factors dissipate thermal energy into the atmosphere and are necessarily considered in this study. The corresponding boundary conditions for external surfaces are:

$$q_c = h\left(T - T_a\right) \tag{8}$$

$$q_r = \varepsilon_r\sigma_r\left(T^4 - T_a^4\right) \tag{9}$$

where h is the heat transfer coefficient of natural thermal convection, which is assumed to be 50 W/m^2·°C; σ_r is the Stefan–Boltzmann constant setting as 5.67×10^{-8} W/m^2•K^4;

and ε_r is the material emissivity setting as 0.3. The base plate underneath the substrate can absorb heat rapidly in the laser deposition process and maintain at ambient temperature. Therefore, in the simulation, the flux boundary is set for the substrate base surface as Eq. (8). By fitting simulated and experimental results, the heat transfer coefficient used for Newton's model is set to 100 W/m^2·°C. In the structural analysis, the internal surface of the gear is set to a fixed boundary condition, i.e., the displacement of all nodes of the surface along the x, y, and z directions is zero.

4.5 Thermo-physical and mechanical properties

The thermo-physical properties and mechanical properties of SS304L were temperature-dependent and identified in [34, 35], as shown in Tables 2–3.

5 Simulation results

5.1 Temperature validation with experiment

Figure 6 shows the simulated temperature history at points A and B where they are located at two end sides on the base substrate, 2 mm upon the tooth root, same location with the thermocouples of TC1 and TC2. The locations are shown in Fig. 6a. Thermocouples were attached on the substrate with thermally conductive paste, and the temperature was recorded with a data acquisition instrument connected to the computer monitor. The predicted temperature history has reheating and cooling stages during the deposition of all layer tracks. The temperature evolution in simulation and the experiments at thermocouples TC1 and TC2 during the actual manufacturing process are compared and presented in Figure 6b. It is observed that simulation has the same trend as the experimental measurement. Good agreement is achieved. The laser scanning outline contour with a zigzag infill pattern was used. That is, laser scans along the z-axis and then follows a zigzag pattern. The tool path was referred to by the extracted points in Fig. 3d. Thermocouples TC1 and TC2 are pasted at two sides of the scanning path. That can explain out of phase results in Fig. 6(b) for points A and B.

Figure 7a shows the temperature contour where the laser is applied to the end of the 1st track, followed by the 4th, 16th, and 28th track in Fig. 7b, c and d. Because of the lower thermal conductivity within the small mass structure compared to the large support base, heat conduction from the heating area to the support base is considerably slower. This leads to a higher temperature in the small heating area. Because of the zigzag infill pattern, the deposited track experiences an alternating sequence of heating and cooling. The transient temperature varies from the ambient temperature to a high temperature (even higher than the melting temperature) and then cools down. The deposited wall has temperature variation from ambient temperature to 1846 °C in the first track. Measured from the zone in temperature contours, the depth of the area where the temperature was

Table 2 Thermo-mechanical properties of the stainless steel 304L substrate

Temperature (°C)	25	100	200	300	400	600	800	1200	1300	1500
Density, (kg/m3)	7900	7880	7830	7790	7750	7660	7560	7370	7320	7320
Thermal conductivity, (W/(mK))	14.6	15.1	16.1	17.9	18	20.8	23.9	32.2	33.7	120
Specific heat, (J/(kgK))	462	496	512	525	540	577	604	676	692	720
Thermal expansion coefficient, (10^{-6}/K)	17	17.4	18	18.6	19	19.6	20	20.7	21.1	21.6
Poisson's ratio	0.29	0.295	0.3	0.31	0.32	0.33	0.34	0.34	0.35	0.39
Elastic modulus, (GPa)	198	193	185	176	167	159	151	60	20	10
Yield strength, (MPa)	265	218	186	170	155	149	91	25	21	10

Table 3 Thermo-mechanical properties of the iron substrate

Temperature (°C)	25	100	200	300	400	600	800	1200	1300	1500
Density, (kg/m3)	7874	7849	7815	7781	7747	7679	7612	7503	7452	7366
Thermal conductivity (W/(mK))	73	68	61	55	49	39	30	35	37	36
Specific heat, (J/(kgK))	450	496	512	525	540	577	604	676	692	720
Thermal expansion coefficient, (10^{-6}/K)	15	15	15	15	15	15	15	15	15	15
Poisson's ratio	0.3	0.3	0.3	0.3	0.3	0.3	0.3	0.3	0.3	0.3
Elastic modulus, (GPa)	199	194	185	174	161	127	84	2	1	1
Yield strength, (MPa)	265	218	186	170	155	149	91	25	21	10

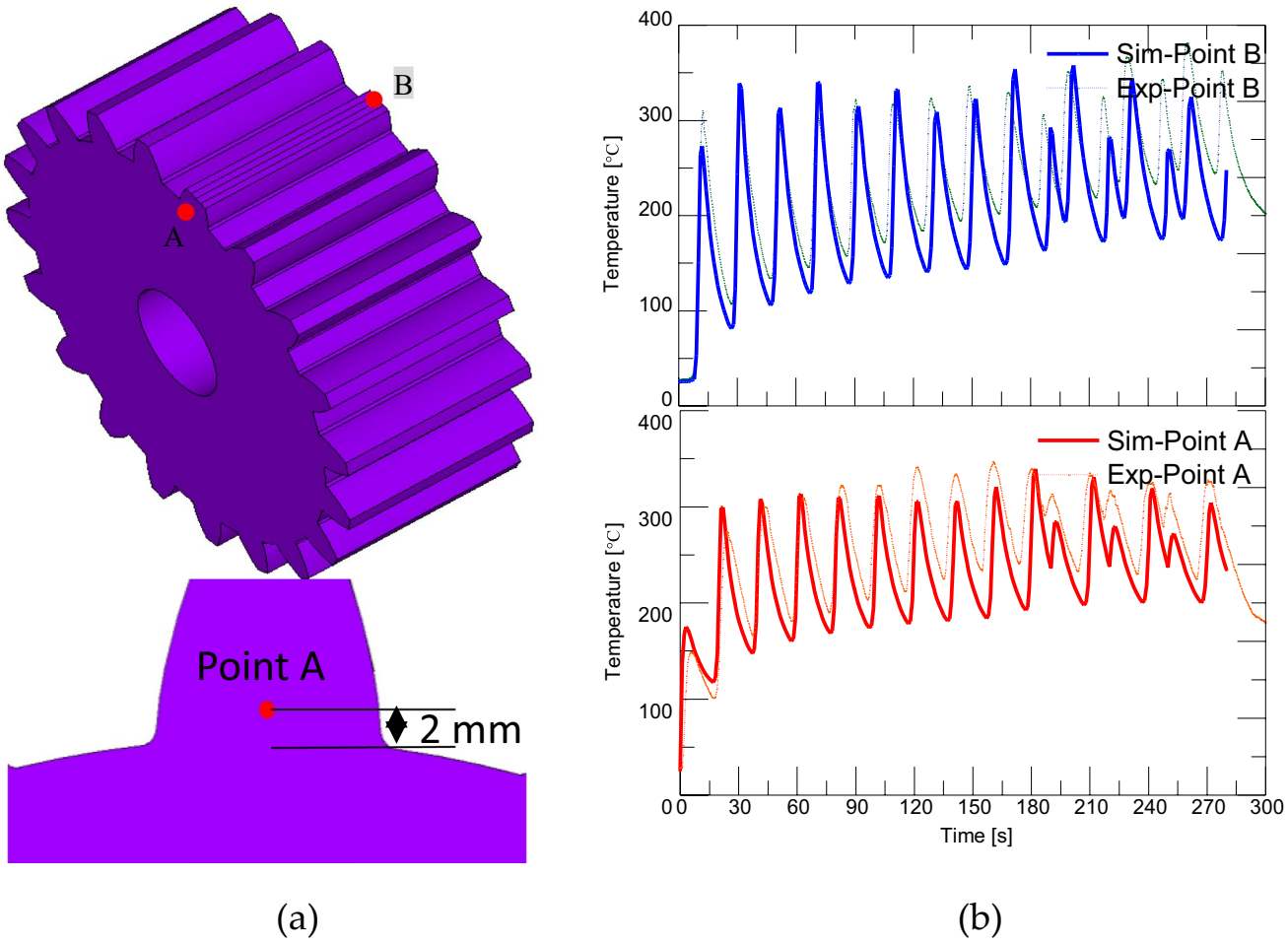

Fig. 6 (**a**) Location of Point A and B. (**b**) The simulated and measured temperature history during the deposition at each selected position, Point A and B

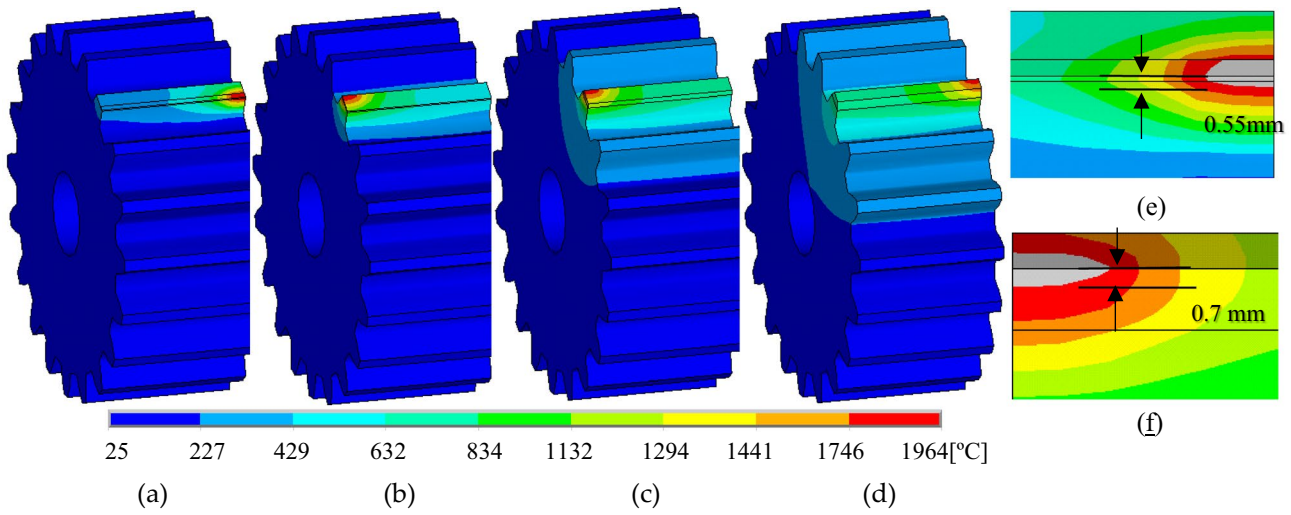

Fig. 7 Temperature distribution at the middle of the n^{th} track, n is 1 (**a**), 4 (**b**), 16 (**c**), and 28 (**d**). Zoom in of temperature contour at the end of 1st in (**e**) and 28th in (**f**) track to measure the melt pool depth

higher than the melting point is 0.55 mm. In Fig. 7e, the zone encompassed by the grey color depicted the molten pool. It can be observed that the melting depth was deep enough to fully bond the first deposited layer and the base substrate. Because of a thermal accumulation from the previous deposition track, the highest temperature raised to 1889 °C at the end of the 4th track in Fig. 7b. Considerably higher temperatures are observed after the deposition of the last track, with the value of 1964 °C in the 28th track as seen in Fig. 7d. Again, the melting depth of 0.7 mm makes fully metallurgical bonding in Fig. 7f. This is because of the heat accumulation effect for additional layers of the successive deposition. In the LDMD process, when printing the upper layer, heat will transfer to the substrate, since the substrate acts as a heat sink in this situation. Therefore, when the deposited layer goes upper, the peak temperature of the upper layers increases.

5.2 Residual stress analysis in simulation

Laser melting trajectory can significantly affect the mechanical properties of deposits [36]. The back-and-forth laser traveling strategies imposed cyclic thermal heating and resulted in cyclic thermal stress. Thermal stress and deformation could be accumulated by the repeated thermal cycles in the material addition process and result in severe part distortions such as delamination and cracking [37]. Scanning parameters can also significantly affect the residual stress and deformation due to locally non-uniform laser heat. Poor path planning may create high residual stresses, gas pores, and distortion on deposits. High residual tensile stress, usually associated with the LDMD process, may cause cracking due to different thermal expansion coefficients between deposits and substrate [38]. Mechanical strain, plastic deformation, and high thermal stresses are important causes of gear damage. Thus, it is important to know the deformation and residual stress distribution of the gear during the repair process.

When all deposition is completed and the component cooled down to ambient temperature, the displacement distributions are illustrated in Fig. 8a-d. The displacement in the x-direction, y-direction (building up direction), z-direction (scanning direction), and total displacement vector are presented in sequence. The final displacement in the y-direction (building up direction) increases with increased layer numbers, and the peak value occurs at or near the free surface of the final deposited layer. This is shown in Fig. 8b at the upper deposition region of the building part, with values of 0.035 mm, whereas the total displacement vector in Fig. 8d has the maximum displacement value on the top free surface of the final deposited layer.

Subsequently, the residual stress distributions are illustrated in Fig. 8e–h. The residual stress in the *x*-direction, *y*-direction (building up direction), *z*-direction (scanning direction), and von Mises stress is presented in sequence. The *z*-component of tensile residual stress in Fig. 8g has a value of 325 MPa near the top surface of the deposited layer, which is highest in all three directions. It is observed that residual stresses are larger along the scan direction than the perpendicular direction due to the larger thermal gradient along the scan direction. This can be explained by the fact that the latest melted and solidified material is subjected to the highest tensile stress when adding new materials. In this regard, the underneath parts are in compression caused by the cooling and contraction of the overlying new molten material. The residual stress in the *x*-direction and *y*-direction (building up direction) implies that the residual stress profile is made up of a large number of tensile stresses at the interface region of the deposits to the base part, whose value is up to 180MPa. This means the deposition strategy and track length also have a large influence on residual stress levels. It is well known that residual stress contributes to the crack formation in the part, which is not acceptable when printing the damaged part. Sometimes delamination of the supports at the intersection position can be observed in the printing field. High residual tensile stress could result in cracking due to different thermal expansion coefficients between deposits and substrate material. While in the current research, the average equivalent stresses show values of 165MPa at the interface section on the deposited tracks. That value is smaller than the yield stress of SS304L. The low equivalent stresses will not induce crack or delamination in repair cases. Hence, this laser repairing task can be treated as successful. The thermo-mechanical FEA model further validated that the proposed repair algorithm is successful and efficient for the automated repair of the damaged gear.

5.3 Residual stress validation with experiments

Numerically predicted von Mises stresses are compared with the experimental measurement along Path L (the middle line on the top surface along deposited layer in Fig. 8i), as shown in Fig. 8i–j. Measured von Mises stresses were obtained using XRD with sin2ψ technique [39]. In XRD measurement, the residual stress is calculated from diffraction line displacement. When residual stress emerges in the sample, the interval between lattice planes will change. This can be manifested by the diffraction peak shift, and the shift distance depends on the residual stress level. As X-rays scan the sample, this stress-induced diffraction shift can be measured by the change of diffraction angle 2θ. The stress is calculated from the slope of 2θ to sin2ψ, where ψ is orientation between normal to the diffracting lattice planes and the sample surface. In the FEA simulation, the stress curve can be readily extracted. Figure 8j shows that residual

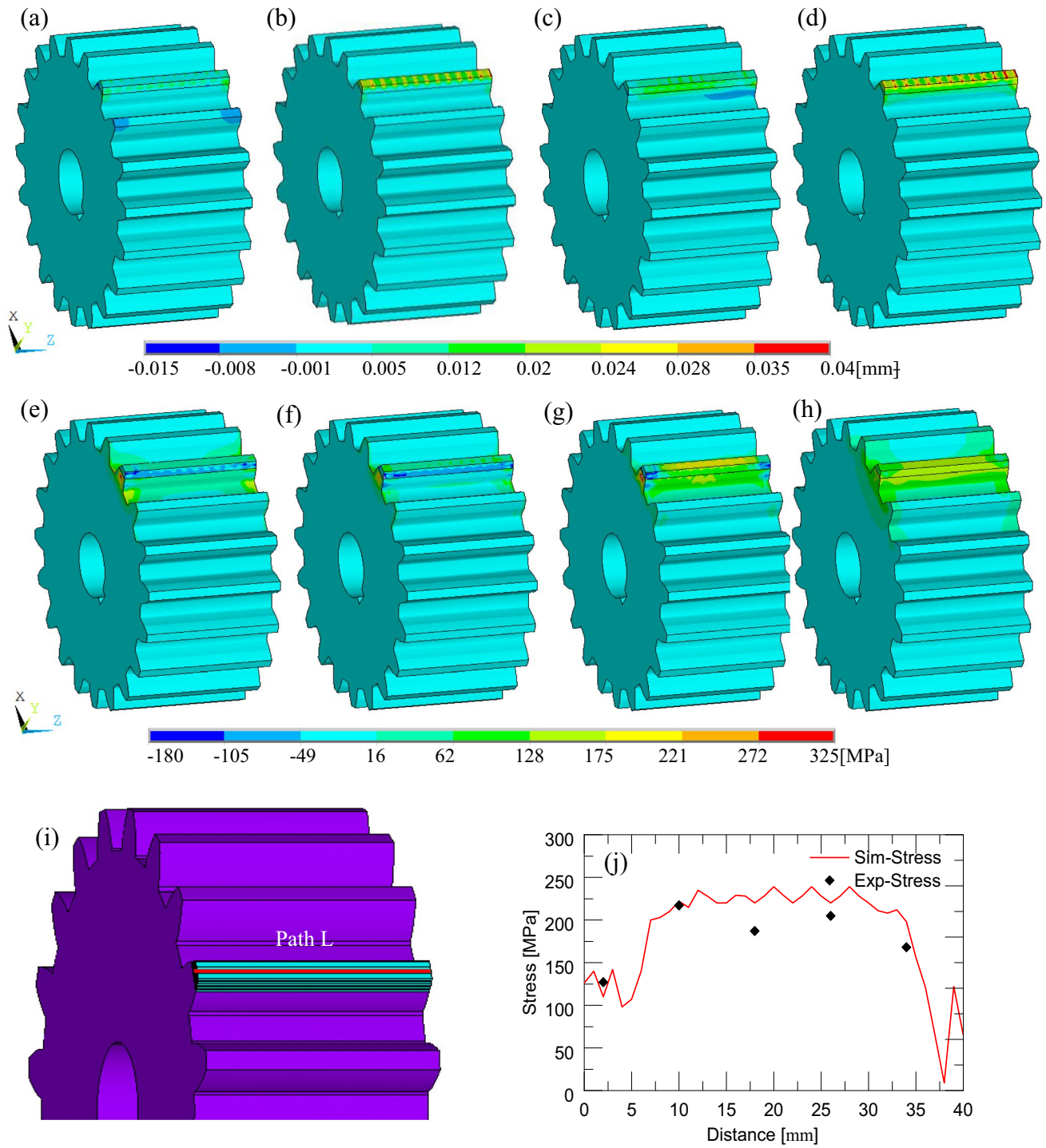

Fig. 8 (**a**) Longitudinal displacement, Ux. (**b**) Transversal displacement, Uy. (**c**) Normal displacement, Uz. (**d**) Displacement vector sum, Usum. (**e**) Longitudinal stress, Sx. (**f**) Transversal stress, Sy. (**g**) Normal stress, Sz. (**h**) Von Mises stress, Seqv, after all deposition done until cooling to room temperature. (**i**) The monitoring locations of Path L, the middle point on the top surface along with layer 8. (**j**) Comparison of experimentally measured and numerically computed von Mises stress along Path L

stress presents the greatest magnitude underneath the wall center and decreases as close to the wall end. Overall, the numerical and experimental curves show fairly good agreement. It can be concluded that simulation can successfully duplicate the stress evolution as experiments for laser repairing in the LDMD process.

6 Conclusions

This work presented an advanced automated damage detection and damage reconstruction algorithm for a damaged gear tooth repair. The defective geometry of the damaged model was detected and compared with the nominal model. Then the damaged model was aligned with the nominal model. After that, both models were sliced into layers, and a set of parallel and equidistant casting rays was used to intersect with these layers to extract the repair volume. Based on the reconstructed 3D model of the gear, a processing strategy was developed to perform precision deposition on the repaired position to accurately restore the gear geometry. This advanced damage detection method fulfills fast and automated repair for complicated geometries.

Then, SS304L powder particles were deposited on the damaged region using the laser-aided direct metal deposition (LDMD) process to validate the repair through the proposed damage reconstruction method. The high coincidence of scanning points between repaired model and nominal model conforming the strong efficiency of this repair algorithm for complex geometry repair. In terms of repair duration, this automated damage reconstruction strategy is time-saving than the conventional method. Microstructure analysis and hardness were carried out to evaluate the quality of the repaired part. Micrographs taken at cross-section near the bonding area were noticed at good metallurgical bonding, and fabrication defects such as delamination, pores, and cracks were not detected in microstructure analysis. These repair experiments confirmed the high efficiency and high quality of the proposed repair algorithm.

Finally, a 3D finite element model based on thermo-mechanical analysis was developed to simulate the LDMD process of the gear repair process, for accurately predicting deformation and stress behavior of the repair process. It was observed that residual stresses are larger along the scan direction than the perpendicular direction. The average equivalent stresses show lower values than the yield stress. The thermo-mechanical FEA model further validated that the proposed repair algorithm is successful and efficient for the automated repair of the damaged gear.

Acknowledgments This project was supported by National Science Foundation Grants CMMI-1547042 and CMMI 1625736, and the Intelligent Systems Center, Center for Aerospace Manufacturing Technologies, and Material Research Center at Missouri S&T. Their financial support is greatly appreciated.

Funding This project was funded by US National Science Foundation [grants numbers CMMI-1547052, CMMI-1625736]. We also appreciate the financial support provided by the Center for Advanced Manufacturing Technologies and Intelligent Systems Center at the Missouri S&T.

Data availability The data that support the findings of this study are available on request.

Code availability Code can be partially shared upon request.

Declarations

Ethics approval Not applicable.

Consent to participate Not applicable.

Consent for publication Not applicable.

Conflicts of interest The authors declare no competing interests.

References

1. Zhang X, Li W, Adkison KM, Liou F (2018) Damage reconstruction from tri-dexel data for laser-aided repairing of metallic components. Int J Adv Manuf Technol 96:3370–3390
2. Davis JR (2005) Gear Materials, Properties, and Manufacture. ASM International, 2005. ISBN: 978-0-87170-815-1
3. Zhang X, Li W, Cui W, Liou F (2018) Modeling of worn surface geometry for engine blade repair using Laser-aided Direct Metal Deposition process. Manuf Lett 15:1–4
4. Gao J, Folkes J, Yilmaz O, Gindy N (2005) Investigation of a 3D non-contact measurement based blade repair integration system. Aircr Eng Aerosp Technol 77:34–41
5. Pantazopoulos G, Zormalia S (2011) Analysis of the failure mechanism of a gripping tool steel component operated in an industrial tube draw bench. Eng Fail Anal 18:1595–1604
6. Grum J, Slabe JM (2003) A comparison of tool–repair methods using CO2 laser surfacing and arc surfacing. Appl Surf Sci 208–209:424–431
7. Pleterski M, Tušek J, Kosec L et al (2010) Laser repair welding of molds with various pulse shapes. Metalurgija 49:41–44
8. Song J, Deng Q, Chen C et al (2006) Rebuilding of metal components with laser cladding forming. Appl Surf Sci 252:7934–7940
9. Nowotny S, Scharek S, Beyer E, Richter K-H (2007) Laser beam build-up welding: Precision in repair, surface cladding, and direct 3D metal deposition. J Therm Spray Technol 16:344–348
10. Rafi HK, Starr TL, Stucker BE (2013) A comparison of the tensile, fatigue, and fracture behavior of Ti – 6Al – 4V and 15-5 PH stainless steel parts made by selective laser melting. Int J Adv Manuf Technol 69:1299–1309
11. Al-Jamal OM, Hinduja S, Li L (2008) Characteristics of the bond in Cu–H13 tool steel parts fabricated using SLM. CIRP Ann 57:239–242
12. Pinkerton AJ, Wang W, Li L (2008) Component repair using laser direct metal deposition. Proc Inst Mech Eng Part B J Eng Manuf 222:827–836
13. Wilson JM, Piya C, Shin YC et al (2014) Remanufacturing of turbine blades by laser direct deposition with its energy and environmental impact analysis. J Clean Prod 80:170–178
14. Graf B, Gumenyuk A, Rethmeier M (2012) Laser metal deposition as repair technology for stainless steel and titanium alloys. Phys Procedia 39:376–381
15. Paydas H, Mertens A, Carrus R et al (2015) Laser cladding as repair technology for Ti–6Al–4V alloy: Influence of building strategy on microstructure and hardness. Mater Des 85:497–510
16. Liu R, Wang Z, Sparks T et al (2017) Stereo vision-based repair of metallic components. Rapid Prototyp J 23:65–73

17. Song L, Zeng G, Xiao H et al (2016) Repair of 304 stainless steel by laser cladding with 316L stainless steel powders followed by laser surface alloying with WC powders. J Manuf Process 24:116–124
18. Zhang X, Li W, Adkison KM, Liou F (2018) Damage reconstruction from tri-dexel data for laser-aided repairing of metallic components. Int J Adv Manuf Technol 96:3377–3390
19. Zhang X, Li W, Liou F (2018) Damage detection and reconstruction algorithm in repairing compressor blade by direct metal deposition. Int J Adv Manuf Technol 95:2393–2404
20. Zhang X, Pan T, Li W et al (2019) Experimental Characterization of a Direct Metal Deposited Cobalt-Based Alloy on Tool Steel for Component Repair. JOM 71:946–955
21. Fang G, Matte C-D, Scharff RBN, Kwok T-H, Wang CCL (2020) Kinematics of Soft Robots by Geometric Computing. IEEE Trans Robot 36(4):1272–1286
22. Ghavidelnia N, Bodaghi M, Hedayati R (2021) Femur Auxetic Meta-Implants with Tuned Micromotion Distribution. Materials 14(1):114
23. Hedayati R, Ghavidelnia N, Sadighi M, Bodaghi M (2021) Improving the Accuracy of Analytical Relationships for Mechanical Properties of Permeable Metamaterials. Appl Sci 11(3):1332
24. Ghavidelnia N, Bodaghi M, Hedayati R (2021) Idealized 3D Auxetic Mechanical Metamaterial: An Analytical, Numerical, and Experimental Study. Materials 14(4):993
25. Li L, Zhang X, Cui W et al (2020) Temperature and residual stress distribution of FGM parts by DED process: modeling and experimental validation. Int J Adv Manuf Technol 109:451–462
26. Li Q, Balachander G, Yao F, Liu GR (2020) Prediction of Thermal Residual Stress and Microstructure in Direct Laser Metal Deposition via a Coupled Finite Element and Multiphase Field Framework. JOM 72(1):496–508
27. Mukherjee T, Zuback JS, Zhang W, DebRoy T (2018) Residual stresses and distortion in additively manufactured compositionally graded and dissimilar joints. Comput Mater Sci 143:325–337
28. Yang Q, Pu Z, Lin C, Zheng M, Minking C, To AC (2016) Finite element modeling and validation of thermomechanical behavior of Ti-6Al-4V in directed energy deposition additive manufacturing. Addit Manuf 12:169–177
29. Megahed M, Mindt H-W, N'Dri N, Duan H, Desmaison O (2016) Metal additive manufacturing process and residual stress modeling. Integrat Mater Manuf Innov 5:1–33
30. Peyre P, Aubry P, Fabbro R, Neveu R, Longuet A (2018) Analytical and numerical modelling of the direct metal deposition laser process. J Phys D Appl Phys 41:025403
31. Jeff Irwin P, Michaleris A (2016) Line Heat Input Model for Additive Manufacturing. J Manuf Sci Eng 138(11):111004
32. ANSYS Theory Manual, Release 8.1, ANSYS Inc., USA, 2004
33. Sigmund O (2011) Notes and Exercises for the Course:FEM-Heavy (41525). Technical University of Denmark
34. Mills KC (2002) Recommended values of thermophysical properties for selected commercial alloys. Woodhead Publishing
35. Li L, Lough C, Replogle A et al (2017) Thermal modeling of 304L stainless steel selective laser melting. In: Proceedings of the ASME 2017 International Mechanical Engineering Congress and Exposition. Advanced Manufacturing, Tampa, FL, USA, pp 1068–1081
36. Shamsaei N, Yadollahi A, Bian L, Thompson SM (2015) An overview of Direct Laser Deposition for additive manufacturing; Part II: Mechanical behavior, process parameter optimization and control. Addit Manuf 8:12–35
37. Cheng B, Shrestha S, Chou K (2016) Stress and deformation evaluations of scanning strategy effect in selective laser melting. Addit Manuf 12:240–251
38. Lin WC, Chen C (2006) Characteristics of thin surface layers of cobalt-based alloys deposited by laser cladding. Surf Coat Technol 200:4557–4563. https://doi.org/10.1016/j.surfcoat.2005.03.033
39. Prevey PS (1986) X-ray diffraction residual stress techniques. ASM Int ASM Handbook 10:380–392